

Coexistence of intrinsic piezoelectricity, ferromagnetism and nontrivial band topology in Li-decorated Janus monolayer Fe_2SSe with high Curie temperature

San-Dong Guo¹, Wen-Qi Mu¹, Meng-Yuan Yin¹, Yu-Chen Li¹ and Wencai Ren^{2,3}

¹*School of Electronic Engineering, Xi'an University of Posts and Telecommunications, Xi'an 710121, China*

²*Shenyang National Laboratory for Materials Science, Institute of Metal Research, Chinese Academy of Sciences, Shenyang 110016, China and*

³*School of Materials Science and Engineering, University of Science and Technology of China, Shenyang 110016, China*

Recently, the quantum anomalous Hall (QAH) insulators are predicted in Lithium-decorated iron-based superconductor monolayer materials (LiFeX ($X=\text{S}, \text{Se}$ and Te)) with very high Curie temperature (PRL 125, 086401 (2020)), which combines the topological and ferromagnetic (FM) orders. It is interesting and useful to achieve coexistence of intrinsic piezoelectricity, ferromagnetism and nontrivial band topology in single two-dimensional (2D) material, namely 2D piezoelectric quantum anomalous hall insulator (PQAH). In this work, 2D Janus monolayer $\text{Li}_2\text{Fe}_2\text{SSe}$ is predicted to be a room-temperature PQAH, which possesses dynamic, mechanical and thermal stabilities. It is predicted to be a half Dirac semimetal without spin-orbit coupling (SOC). It is found that the inclusion of SOC opens up a large nontrivial gap, which means the nontrivial bulk topology (QAH insulator), confirmed by the calculation of Berry curvature and the presence of two chiral edge states (Chern number $C=2$). Calculated results show that monolayer $\text{Li}_2\text{Fe}_2\text{SSe}$ possesses robust QAH states against biaxial strain and electronic correlations. Compared to LiFeX , the glide mirror G_z of $\text{Li}_2\text{Fe}_2\text{SSe}$ disappears, which will induce only out-of-plane piezoelectric response. The calculated out-of-plane d_{31} of monolayer $\text{Li}_2\text{Fe}_2\text{SSe}$ is -0.238 pm/V comparable with ones of other 2D known materials. Moreover, very high Curie temperature (about 1000 K) is predicted by using Monte Carlo (MC) simulations, which means that the QAH effect can be achieved at room temperature in Janus monolayer $\text{Li}_2\text{Fe}_2\text{SSe}$. Similar to monolayer $\text{Li}_2\text{Fe}_2\text{SSe}$, the PQAH can also be realized in the Janus monolayer $\text{Li}_2\text{Fe}_2\text{SeTe}$. Our works open a new avenue in searching for PQAH with high temperature and high Chern numbers, which provide a potential platform for multi-functional spintronic applications.

PACS numbers: 71.20.-b, 77.65.-j, 72.15.Jf, 78.67.-n

Email:sandongyuwang@163.com

Keywords: Ferromagnetism, Piezoelectronics, Topological insulator, Janus monolayer

I. INTRODUCTION

The quantum Hall (QH) effect can be achieved in a 2D electron gas by a strong perpendicular external magnetic field¹, while the occurrence of the QAH effect arises from SOC and time-reversal (TR) symmetry broken in the presence of magnetic order². The QAH effect is generally confirmed by a nonzero Chern number in accordance with the number of edge states, and only one spin species are allowed to flow unidirectionally, resulting in a quantized Hall conductance³⁻⁵. The discovery of TR invariant topological insulators promotes the experimental realization of QAH effect^{6,7}. Following the theoretical work⁸, the QAH effect is achieved experimentally in thin films of Cr doped $(\text{Bi}, \text{Sb})_2\text{Te}$ below 30 mK, with quantized Hall conductance being observed⁹. The QAH effect achieves the coexistence of magnetism and topological electronic band structure in a single compound. It's a natural idea to combine more properties in a material, like the coexistence of QAH effect and piezoelectricity.

The piezoelectricity of 2D materials has been widely investigated in recent years¹⁰. The piezoelectricity of 2D materials has been observed experimentally¹¹⁻¹⁴, and the density functional theory (DFT) calculations have also predicted the piezoelectric properties of many 2D materials¹⁵⁻²⁴, which lack centrosymmetry. Recently, some 2D multifunctional piezoelectric materials have

been predicted by the first-principle calculations. In the 2D vanadium dichalcogenides, VSi_2P_4 , $\text{CrBr}_{1.5}\text{I}_{1.5}$ and InCrTe_3 ²⁵⁻²⁸, the piezoelectric ferromagnetism (PFM) has been predicted, which combines piezoelectricity and ferromagnetism. The combination of piezoelectricity with topological insulating phase, namely piezoelectric quantum spin Hall insulator (PQSHI), has also been realized in monolayer InXO ($X=\text{Se}$ and Te)²⁹ and Janus monolayer SrAlGaSe_4 ³⁰. These discoveries provide possibility for using piezoelectric effect to control the quantum or spin transport process, which may induce novel device applications or scientific breakthroughs.

In fact, in our recent work, the PQAH has also been achieved in Janus monolayer Fe_2IX ($X=\text{Cl}$ and Br)³¹, based on QAH insulator Fe_2I_2 ³². Recently, the lithium decoration of layered iron-based superconductor materials FeX ($X=\text{S}, \text{Se}$ and Te), namely LiFeX , are predicted as room-temperature QAH insulators with high Chern number ($C=2$)³³, and the guidances on experimental realization have also been discussed. The LiFeX ($X=\text{S}, \text{Se}$ and Te) have similar crystal structure with Fe_2I_2 , and no piezoelectricity can be observed due to inversion symmetry. A natural idea is to achieve PQAH from LiFeX ($X=\text{S}, \text{Se}$ and Te) monolayer by removing inversion symmetry. As an example, the monolayer FeSe has particular sandwiched structure (Se-Fe-Se), and Janus structure can be built by replacing the top Se atomic layer with S

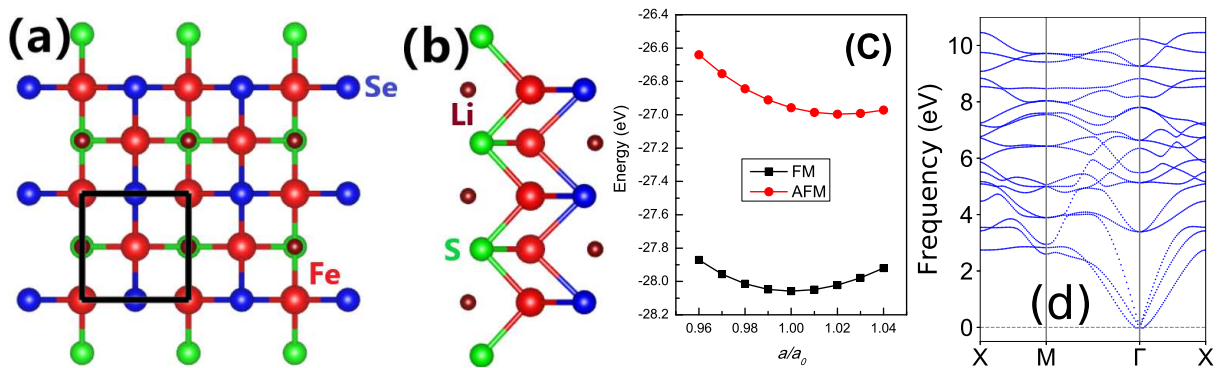


FIG. 1. (Color online) The (a) top view and (b) side view of crystal structure of Janus monolayer $\text{Li}_2\text{Fe}_2\text{SSe}$. The black frame represents the primitive cell. (c): The FM and AFM energy of Janus monolayer $\text{Li}_2\text{Fe}_2\text{SSe}$ as a function of a/a_0 . (d): The phonon band dispersions of Janus monolayer $\text{Li}_2\text{Fe}_2\text{SSe}$ with FM order.

atoms (Fe_2SSe), and then apply the gating techniques to inject a large amount of Li ions into monolayer Fe_2SSe ($\text{Li}_2\text{Fe}_2\text{SSe}$). The related experimental techniques have been widely used^{34–38}.

In this work, it is found that, by first-principles calculations, Janus monolayer $\text{Li}_2\text{Fe}_2\text{SSe}$ is a 2D ferromagnetic semiconductor with out-of-plane magnetization, which can achieve the QAH effect at quite high temperature. Janus monolayer $\text{Li}_2\text{Fe}_2\text{SSe}$ is proved to be dynamically, mechanically and thermally stable. According to the results of Berry curvature and Chiral edge states, a high Chern number $C=2$ is obtained for $\text{Li}_2\text{Fe}_2\text{SSe}$. It is found that QAH effect of $\text{Li}_2\text{Fe}_2\text{SSe}$ is robust against biaxial strain and electronic correlations. A very high Curie temperature of about 1000 K is estimated by MC simulations using Heisenberg model. A particular symmetry leads to only out-of-plane piezoelectric response, and the predicted out-of-plane d_{31} is -0.238 pm/V, which is comparable with ones of other 2D known materials. These results indicate that 2D Janus $\text{Li}_2\text{Fe}_2\text{SSe}$ may be promising candidate for realizing the room-temperature PQAH in experiments, which is very useful for developing 2D piezoelectric spin topological devices.

The rest of the paper is organized as follows. In the next section, we shall give our computational details and methods. In the next few sections, we shall present crystal structure, structural stabilities, topological properties, strain and correlation effects on topological properties, Curie temperature and piezoelectric properties of 2D Janus $\text{Li}_2\text{Fe}_2\text{SSe}$. Finally, we shall give our discussion and conclusions.

II. COMPUTATIONAL DETAIL

All the calculations on the elastic, electronic, topological and piezoelectric properties are based on DFT³⁹, as implemented in the VASP code^{40–42}. The projector-augmented-wave (PAW) potential and the plane-wave basis with a kinetic energy cutoff of 500 eV are employed

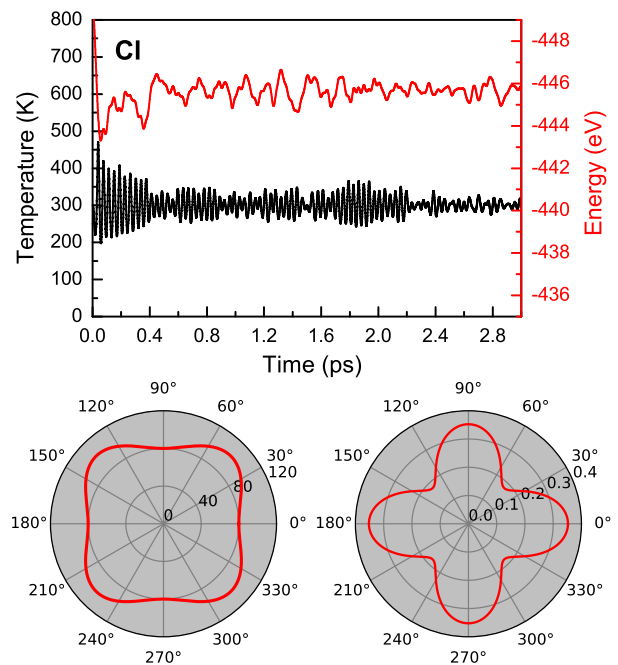


FIG. 2. (Color online) Top: the temperature and total energy fluctuations of Janus monolayer $\text{Li}_2\text{Fe}_2\text{SSe}$ with FM order at 300 K. Bottom: the angular dependence of the Young's modulus ($C_{2D}(\theta)$) and Poisson's ratio ($\nu_{2D}(\theta)$) of Janus monolayer $\text{Li}_2\text{Fe}_2\text{SSe}$.

for Janus monolayer $\text{Li}_2\text{Fe}_2\text{SSe}$. We use popular generalized gradient approximation (GGA) of Perdew, Burke and Ernzerhof⁴³ as the exchange-correlation functional, and the SOC is included by a second variational procedure on a fully self-consistent basis. The total energy convergence criterion is set for 10^{-8} eV with the Gaussian smearing method. The force convergence criterion is set for less than 0.0001 eV.Å⁻¹ for optimizing the lattice constants and atomic coordinates by the conjugate gradient (CG) scheme. To avoid artificial interactions caused by the periodic boundary condition, the vacuum layer is

set to more than 15 Å. The Fe-3d orbitals generally have important correlation effects, and the DFT+ U method⁴⁴ is employed for the treatment of the strongly correlated 3d electrons with $U_{eff} = 2.5$ eV^{32,45}.

With FM ground state, the interatomic force constants (IFCs) with the $5 \times 5 \times 1$ supercell are calculated through the direct supercell method. Based on harmonic IFCs, the phonon dispersions are attained by using Phonopy code⁴⁶. An effective tight-binding Hamiltonian constructed from the maximally localized Wannier function (MLWF) is used to calculate the surface states and Berry curvature with the iterative Green function method, as implemented in the package WannierTools^{47,48}. The Curie temperature is determined by MC simulations, as implemented by Mcsolver code⁴⁹.

The elastic stiffness tensor C_{ij} and piezoelectric stress tensor e_{ij} are carried out by using strain-stress relationship (SSR) with GGA and density functional perturbation theory (DFPT) method⁵⁰ using GGA+SOC. The Brillouin zone (BZ) integration is sampled by using a $18 \times 18 \times 1$ Monkhorst-Pack grid for the self-consistent calculations and elastic coefficients C_{ij} . A very dense mesh of $26 \times 26 \times 1$ k-points in the BZ is adopted to attain the accurate e_{ij} . The 2D elastic coefficients C_{ij}^{2D} and piezoelectric stress coefficients e_{ij}^{2D} have been renormalized by $C_{ij}^{2D} = Lz C_{ij}^{3D}$ and $e_{ij}^{2D} = Lz e_{ij}^{3D}$, where the Lz is the length of unit cell along z direction.

III. CRYSTAL STRUCTURE

The FeSe monolayer has Se-Fe-Se trilayers with a tetragonal lattice in the $P4/nmm$ space group, the unit cell of which contains four atoms with two co-planar Fe atoms. It is proved that the room-temperature QAH insulator can be achieved by Li decoration of FeSe monolayer³³. In fact, the Fe_2I_2 monolayer, having the same crystal structure with FeSe, is predicted to be a QAH insulator³². The I element has one more valence electron than Se element, and the Li atom with an ultralow electronegativity easily loses one valence. So, the Li decoration of FeSe monolayer can become a QAH insulator. It is well known that Janus monolayer MoSSe (S-Mo-Se) can be constructed from $MoSe_2$ with three atomic sublayers (Se-Mo-Se)³⁴. In our previous work, the Janus monolayer Fe_2IX ($X=Cl$ and Br) is predicted to be PQAHI³¹, which is built by replacing one of two I layers with X ($X=Cl$ and Br) atoms in monolayer Fe_2I_2 . It is a natural idea to construct Janus Fe_2SSe monolayer (S-Fe-Se) by replacing one of two Se layers with S atoms in monolayer FeSe, and then to achieve PQAHI by Li decoration of Janus monolayer Fe_2SSe (Li_2Fe_2SSe). Compared with FeSe monolayer, the Li_2Fe_2SSe monolayer with $P4mm$ space group (No.99) lacks centrosymmetry, giving rise to piezoelectricity. The top and side views of schematic crystal structure of Janus monolayer Li_2Fe_2SSe are shown in Figure 1.

The ground state of Janus monolayer Li_2Fe_2SSe can be

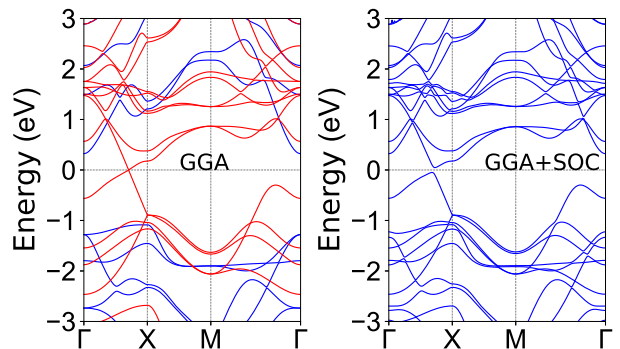


FIG. 3. (Color online) The energy band structures of Janus monolayer Li_2Fe_2SSe without and with SOC at the FM order. The blue (red) lines represent the spin-up (spin-down) bands without SOC.

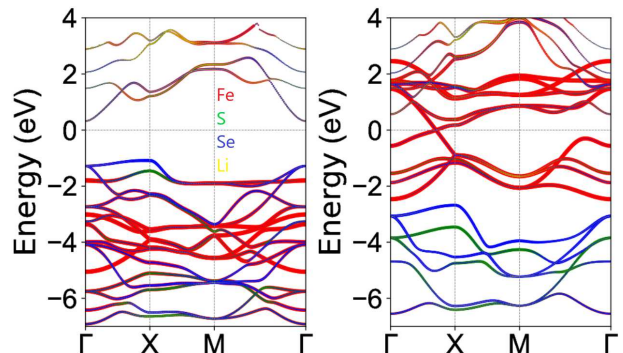


FIG. 4. (Color online) Band structure of Janus monolayer Li_2Fe_2SSe without the SOC for spin up (left) and spin down (right). The contribution of Fe, S, Se and Li atoms to the Bloch states are denoted by red, green, blue and yellow dots.

determined by comparing the energy difference between antiferromagnetic (AFM) and FM states. The magnetic ground state of Li_2Fe_2SSe monolayer is FM, which can be seen from the (c) in Figure 1. The optimized lattice constants a_0 is 3.636 Å with FM order, which is between ones of $LiFeS$ (3.542 Å) and $LiFeSe$ (3.655 Å)³³. The thermal stability of magnetic ordering can be described by the magnetic anisotropy energy (MAE), stemming from the SOC effect. The (100) and (001) directions are used to obtain relative stabilities by using GGA+SOC. The energy difference of the magnetic moments constrained in the (100) and (001) direction is 172 $\mu eV/Fe$, indicating that the out-of-plane (001) direction is the easy one for magnetization in monolayer Li_2Fe_2SSe . A built-in electric field can be produced by the the inequivalent bond lengths and bond angles (see Table I) due to different atomic sizes and electronegativities of S and Se atoms. For $LiFeSe$ monolayer, the key space-group symmetry operations contain space inversion P , C_4 rotation, M_x and M_y mirrors and glide mirror $G_z = \{M_z | \frac{1}{2}, \frac{1}{2}, 0\}$ ³³. For Li_2Fe_2SSe monolayer, besides the missing P , the glide mirror G_z is also removed.

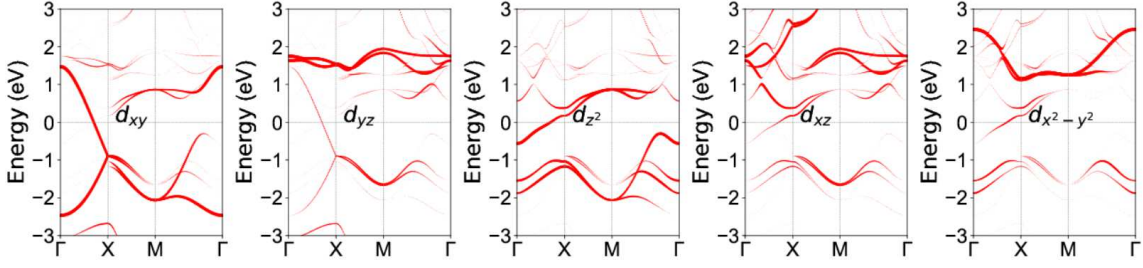


FIG. 5. (Color online) At the absence of SOC, the band structure of Janus monolayer $\text{Li}_2\text{Fe}_2\text{SSe}$ for spin down with the contribution of d_{xy} , d_{yz} , d_{z^2} , d_{xz} and $d_{x^2-y^2}$ orbitals to the Bloch states.

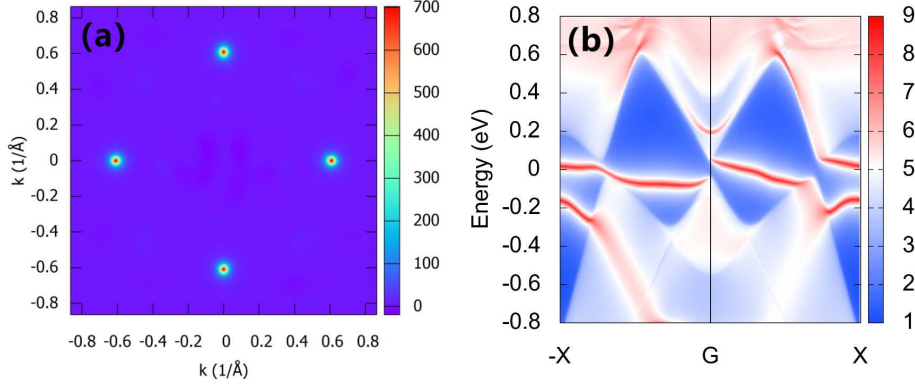


FIG. 6. (Color online) (a): The distribution of Berry curvature of Janus monolayer $\text{Li}_2\text{Fe}_2\text{SSe}$ contributed by occupied valence bands in the momentum space. (b): The topological edge states of $\text{Li}_2\text{Fe}_2\text{SSe}$ calculated along the (100) direction.

TABLE I. For Janus monolayer $\text{Li}_2\text{Fe}_2\text{SSe}$, the lattice constants a_0 (Å); Fe-Se (d_1), Fe-S (d_2), Li-Se (d_3), Li-S (d_4) bond lengths (Å); Se-Fe-Se (θ_1) and S-Fe-S (θ_2) angles; the thickness layer height t (Å); the elastic constants C_{ij} in Nm^{-1} .

a_0	d_1	d_2	d_3	d_4	θ_1
3.636	2.587	2.467	2.599	2.612	89.26
θ_2	t	C_{11}	C_{12}	C_{66}	
94.94	4.347	91.26	32.15	43.00	

IV. STRUCTURAL STABILITY

The phonon calculation of $\text{Li}_2\text{Fe}_2\text{SSe}$ (see (d) in Figure 1) reveals that there are no imaginary frequency modes, confirming its dynamic stability, which means that $\text{Li}_2\text{Fe}_2\text{SSe}$ monolayer can exist as free-standing 2D crystal. A total of 18 branches due to 6 atoms per unitcell can be observed, including 15 optical and 3 acoustical phonon branches. The out-of-plane acoustic (ZA) branch (out-of-plane vibrations) deviates from linearity, in accord with the conclusion that the ZA phonon branch should have quadratic dispersion for the unstrained monolayer^{51,52}. The thermal stability of $\text{Li}_2\text{Fe}_2\text{SSe}$ monolayer is further assessed by performing ab initio molecular dynamics (AIMD) simulations using NVT ensemble with a $4 \times 4 \times 1$ supercell at 300 K. For $\text{Li}_2\text{Fe}_2\text{SSe}$ monolayer, the temperature and total en-

ergy fluctuations as a function of the simulation time are shown in Figure 2. It is found that the total energy and temperature fluctuate smoothly with small amplitudes after the preheating process, which means a favorable thermal stability for $\text{Li}_2\text{Fe}_2\text{SSe}$ monolayer at room temperature.

The mechanical stability of monolayer $\text{Li}_2\text{Fe}_2\text{SSe}$ can be checked by Born criteria of mechanical stability:

$$C_{11} > 0, \quad C_{66} > 0, \quad C_{11} - C_{12} > 0 \quad (1)$$

where the C_{11} , C_{12} and C_{66} are three independent elastic constants. By using Voigt notation, the elastic tensor with $4mm$ point-group symmetry can be reduced into:

$$C = \begin{pmatrix} C_{11} & C_{12} & 0 \\ C_{12} & C_{11} & 0 \\ 0 & 0 & C_{66} \end{pmatrix} \quad (2)$$

The calculated C_{11} , C_{12} and C_{66} are 91.26 Nm^{-1} , 32.15 Nm^{-1} and 43.00 Nm^{-1} , which satisfy the above Born criteria of mechanical stability, indicating mechanical stability of monolayer $\text{Li}_2\text{Fe}_2\text{SSe}$.

Due to C_4 rotation symmetry, the mechanical properties of monolayer $\text{Li}_2\text{Fe}_2\text{SSe}$ have C_4 symmetry, and the direction-dependent in-plane Young's moduli $C_{2D}(\theta)$ and Poisson's ratios $\nu_{2D}(\theta)$ can be attained by^{53,54}:

$$C_{2D}(\theta) = \frac{C_{11}C_{22} - C_{12}^2}{C_{11}m^4 + C_{22}n^4 + (B - 2C_{12})m^2n^2} \quad (3)$$

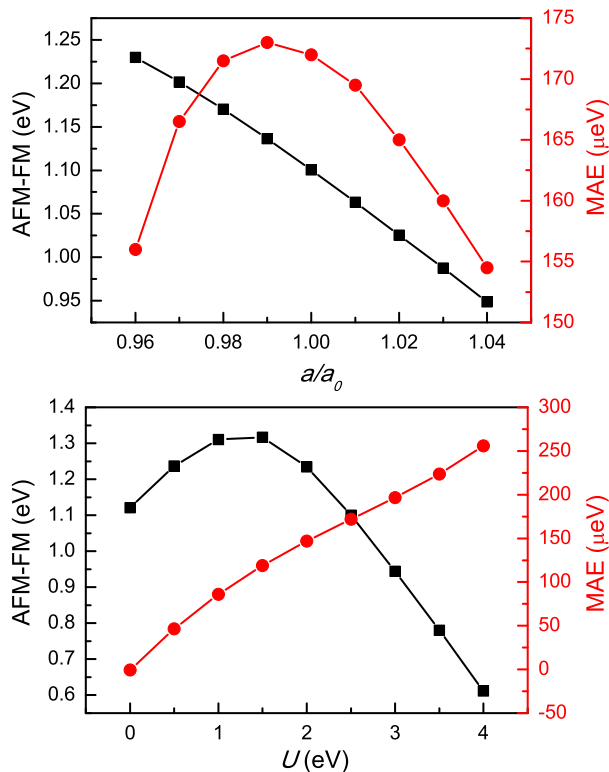


FIG. 7. (Color online) For Janus monolayer $\text{Li}_2\text{Fe}_2\text{SSe}$, the energy difference between FM and AFM order and MAE as a function of a/a_0 (Top) and U (Bottom).

$$\nu_{2D}(\theta) = \frac{(C_{11} + C_{22} - B)m^2n^2 - C_{12}(m^4 + n^4)}{C_{11}m^4 + C_{22}n^4 + (B - 2C_{12})m^2n^2} \quad (4)$$

in which $m = \sin(\theta)$, $n = \cos(\theta)$ and $B = (C_{11}C_{22} - C_{12}^2)/C_{66}$. The θ is the angle of the direction with the x direction as 0° . The $C_{2D}(\theta)$ and $\nu_{2D}(\theta)$ as a function of the angle θ are plotted in Figure 2. It is clearly seen that they show C_4 symmetry, and we only consider the 0° - 90° angle range. The softest direction is along the (100) direction, while the hardest direction is along the (110) direction, and the corresponding Young's moduli is 79.94 Nm^{-1} and 101.36 Nm^{-1} . The maximum value of Young's moduli is less than that of many 2D materials^{15,18,55}, which means that the monolayer $\text{Li}_2\text{Fe}_2\text{SSe}$ has extraordinary flexibility. For Poisson's ratios, the minima is along the (110) direction (0.179), while the maxima is along the (100) direction (0.352).

V. TOPOLOGICAL PROPERTIES

The energy band structures of monolayer $\text{Li}_2\text{Fe}_2\text{SSe}$ with GGA is plotted in Figure 3, along with atom projected band structure in Figure 4. Without SOC, monolayer $\text{Li}_2\text{Fe}_2\text{SSe}$ shows a 2D half Dirac semimetal state with a large-gap insulator for spin up (1.41 eV) and a gapless Dirac semimetal for spin down. Due to C_4 symmetry, the four Dirac cones in the BZ can be observed for spin

down along the mirror symmetry invariant lines Γ -X and Γ -Y. The important observation is that the states around the Fermi level for spin down are dominated by the Fe- d orbitals, which means that the Fe- d orbitals are partially occupied. However, the spin-up channel is fully occupied. These lead to the high-spin state for Fe atom, giving a spin magnetic moment of $3 \mu_B$. To understand the composition of Dirac cone, we project the states to five Fe- d orbitals for spin down, which are plotted in Figure 5. Calculated results show that the states around Dirac cone are dominated by the d_{xy} and d_{z^2} orbital. We then investigate the electronic band structures with SOC, and the energy bands are shown in Figure 3. When including SOC, the Dirac point splits apart with a noticeable energy gap opened, and the corresponding gap is 96.2 meV for $\text{Li}_2\text{Fe}_2\text{SSe}$, which suggests nontrivial topology.

When the TR symmetry of a material breaks with a finite magnetic ordering, the topologically nontrivial properties can be verified by a non-zero Chern number in the valence bands. The Chern number of monolayer $\text{Li}_2\text{Fe}_2\text{SSe}$ can be attained by integrating the Berry curvature ($\Omega_z(k)$) of the occupied bands:

$$C = \frac{1}{2\pi} \int_{\text{BZ}} d^2k \Omega_z(k) \quad (5)$$

$$\Omega_z(k) = \nabla_k \times i \langle \mu_{n,k} | \nabla_k \mu_{n,k} \rangle \quad (6)$$

in which the $\mu_{n,k}$ is the lattice periodic part of the Bloch wave functions. The distributions of Berry curvature of monolayer $\text{Li}_2\text{Fe}_2\text{SSe}$ are shown in Figure 6. As can be observed, the nonzero Berry curvature is mainly distributed around four Dirac cones, and they have the same sign because of C_4 symmetry. Two Berry curvature peaks contribute to the nonzero Chern number 1, and the total Chern number from the 4 Berry curvature peaks equals 2. In other words, a quantized Berry phase of π can be attained for each gapped Dirac cone, and the total Berry phase of 4π is attained (four Dirac cones), giving rise to a Chern number $C=2$.

Based on the bulk-edge correspondence, the non-zero Chern number can be further confirmed by the number of nontrivial chiral edge states inside the bulk gap of a semiinfinite system. The local density of states vs momentum and energy at the edge can be obtained from the imaginary part of the surface Green's function:

$$A(k, \omega) = -\frac{1}{\pi} \lim_{\eta \rightarrow 0^+} \text{ImTr} G_s(k, \omega + i\eta) \quad (7)$$

The topological edge states along the (100) direction are shown in Figure 6. It is clearly seen that the bulk states are connected by two chiral edge states, which indicates that Chern number equals to 2. These results show that monolayer $\text{Li}_2\text{Fe}_2\text{SSe}$ is a QAH insulator.

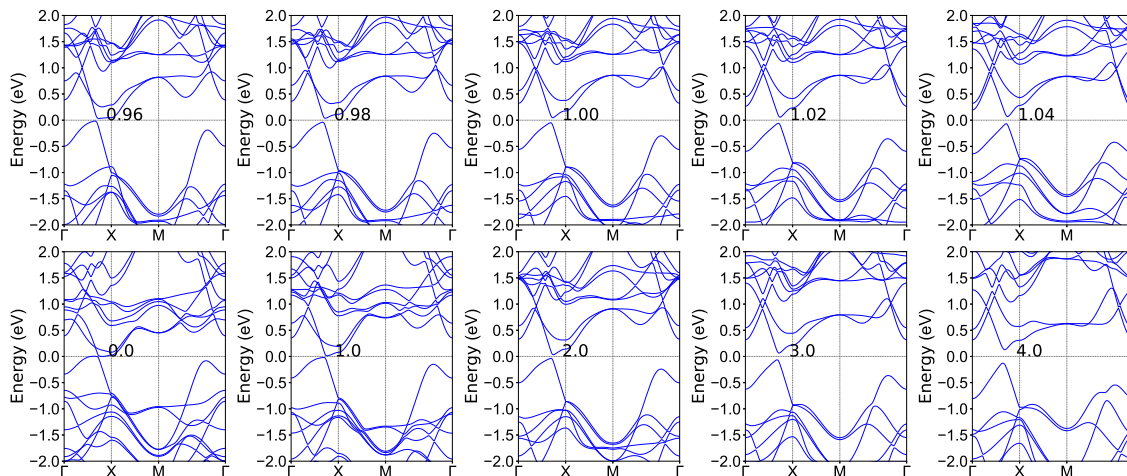


FIG. 8. (Color online) The energy band structures of Janus monolayer $\text{Li}_2\text{Fe}_2\text{SSe}$ using GGA+SOC with five different a/a_0 (Top) and U (Bottom).

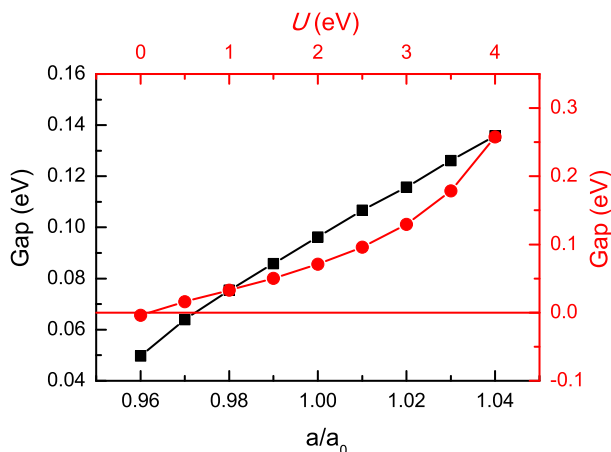


FIG. 9. (Color online) For Janus monolayer $\text{Li}_2\text{Fe}_2\text{SSe}$, the gap as a function of a/a_0 and U using GGA+SOC.

VI. STRAIN AND CORRELATION EFFECTS ON TOPOLOGICAL PROPERTIES

The strain generally can tune the SOC-induced bulk gap, MAE and magnetic order. It is important to investigate robustness of QAH properties of monolayer $\text{Li}_2\text{Fe}_2\text{SSe}$ against biaxial strain. Here, we use a/a_0 (0.96-1.04) to describe the biaxial strain, where a (a_0) is the strained (equilibrium) lattice constants. The energy difference between FM and AFM orders and MAE as a function of a/a_0 are plotted in Figure 7. It is found that all strained monolayers are FM ground state in considered strain range, and the energy difference between FM and AFM order decreases with a/a_0 from 0.96 to 1.04. However, the MAE shows nonmonotonicity, which firstly increases, and then decreases. In considered strain range, the out-of-plane (001) direction is always the easy one. The energy band structures of some representa-

tive strained monolayer $\text{Li}_2\text{Fe}_2\text{SSe}$ using GGA+SOC are plotted in Figure 8, and the gap as a function of strain is shown in Figure 9. It is found that the gap increases almost linearly with increasing strain in considered strain range, and the gap changes from 49.7 meV to 135.8 meV. The topological edge states of strained monolayer $\text{Li}_2\text{Fe}_2\text{SSe}$ are calculated, and they all are QAH insulators with Chern number $C=2$. We show topological edge states at representative 1.04 strain in Figure 10, which shows clearly two chiral topologically protected gapless edge states. These results show that the QAH topological properties of monolayer $\text{Li}_2\text{Fe}_2\text{SSe}$ are robust against strain.

To check the Coulomb interaction U effects on QAH properties, we calculate the energy difference between FM and AFM orders, MAE, energy bands and topological edge states with different values of U (0-4 eV). The energy difference between FM and AFM order and MAE as a function of U are plotted in Figure 7. It is found that the ground state always is FM order with different U . It is found that the MAE increases with increasing U . When the U value is larger than 0 eV, the out-of-plane (001) direction is always the easy one in considered U range. For $U=0$ eV, the MAE only is $-0.5 \mu\text{eV}/\text{Fe}$, and the spin orientation in the energy band calculations is chosen in the out-of-plane direction. The energy band structures of monolayer $\text{Li}_2\text{Fe}_2\text{SSe}$ with some representative U value using GGA+SOC are plotted in Figure 8, and the gap as a function of U is shown in Figure 9. With increasing U , it is clearly seen that the gap increases from -4.1 meV to 257.6 meV. For $U=0$ eV, the monolayer $\text{Li}_2\text{Fe}_2\text{SSe}$ becomes metal. In considered U range except $U=0$ eV, the topological edge states of monolayer $\text{Li}_2\text{Fe}_2\text{SSe}$ are calculated, and they all are QAH insulators with Chern number $C=2$. The topological edge states at representative $U=4$ eV are shown in Figure 10, and two chiral topologically protected gapless edge states are present in the bulk gap. These results indicate the

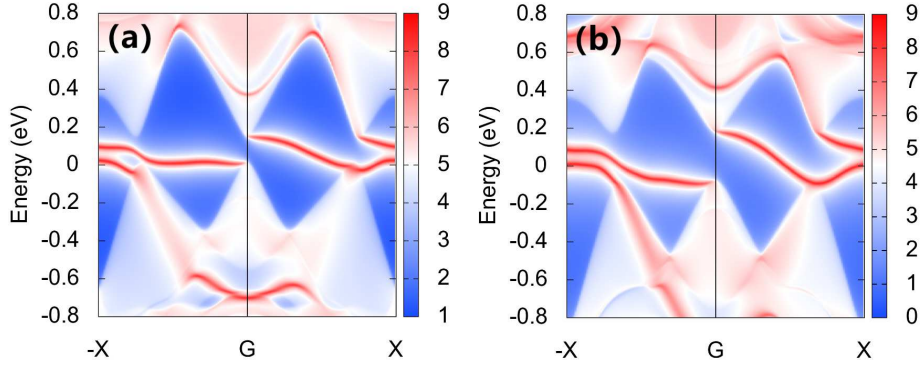


FIG. 10. (Color online) Topological edge states of Janus monolayer $\text{Li}_2\text{Fe}_2\text{SSe}$ calculated along the (100) direction with $a/a_0=1.04$ (a) and $U=4$ eV (b).

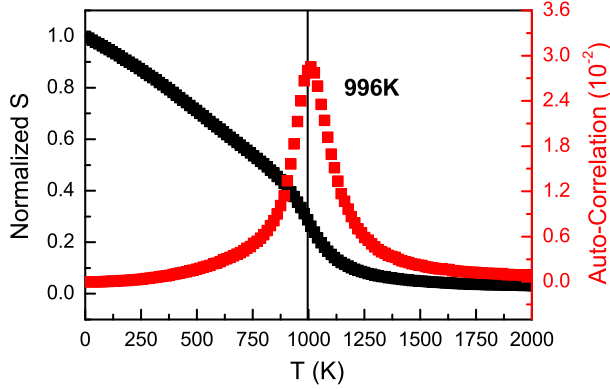


FIG. 11. (Color online) The normalized magnetic moment (S) and auto-correlation of Janus monolayer $\text{Li}_2\text{Fe}_2\text{SSe}$ as a function of temperature.

robustness of nontrivial topology against the correlation effect in the $3d$ electrons of Fe atoms.

VII. CURIE TEMPERATURE

One of the important properties of ferromagnets for the practical application is the Curie temperatures (T_C). Using MC simulations based on the Heisenberg model, we have calculated the Curie temperature of monolayer $\text{Li}_2\text{Fe}_2\text{SSe}$. For simplicity, only the nearest neighbor (NN) exchange interaction is considered, and the spin Heisenberg Hamiltonian is defined as:

$$H = -J \sum_{i,j} S_i \cdot S_j - A \sum_i (S_i^z)^2 \quad (8)$$

where J , S and A are the exchange parameter, the spin vector of each atom and MAE, respectively. Based on the energy difference between AFM and FM, the magnetic coupling parameter is calculated as $J=(E_{AFM}-E_{FM})/8$ with normalized S ($|S|=1$). The calculated J value is 137.6 meV, and the A is 172 $\mu\text{eV}/\text{Fe}$.

A 50×50 supercell with periodic boundary conditions is employed, and 10^7 loops are adopted to perform the MC simulation. We show the normalized magnetic moment and auto-correlation of monolayer $\text{Li}_2\text{Fe}_2\text{SSe}$ as a function of temperature in Figure 11. It is found that T_C is as high as 996 K for monolayer $\text{Li}_2\text{Fe}_2\text{SSe}$, which is smaller than ones of Li-decorated monolayer FeX ($X=$ S, Se and Te)³³. However, the T_C of monolayer $\text{Li}_2\text{Fe}_2\text{SSe}$ is significantly higher than that of previously reported many 2D FM semiconductors, like CrI_3 monolayer (about 45 K)⁵⁶, CrOCl monolayer (about 160 K)⁵⁷, Janus Fe_2IX ($X=\text{Cl}$ and Br) monolayer (about 400 K)³¹, Fe_2I_2 monolayer (about 400 K)³² and $\text{Cr}_2\text{Ge}_2\text{Te}_6$ monolayer (about 20 K)⁵⁸.

VIII. PIEZOELECTRIC PROPERTIES

The piezoelectric effects of a material can be described by third-rank piezoelectric stress tensor e_{ijk} and strain tensor d_{ijk} . The e_{ijk} and d_{ijk} can be expressed as:

$$e_{ijk} = \frac{\partial P_i}{\partial \varepsilon_{jk}} = e_{ijk}^{elc} + e_{ijk}^{ion} \quad (9)$$

and

$$d_{ijk} = \frac{\partial P_i}{\partial \sigma_{jk}} = d_{ijk}^{elc} + d_{ijk}^{ion} \quad (10)$$

They can be related by elastic tensor C_{mnljk} :

$$e_{ijk} = \frac{\partial P_i}{\partial \varepsilon_{jk}} = \frac{\partial P_i}{\partial \sigma_{mn}} \cdot \frac{\partial \sigma_{mn}}{\partial \varepsilon_{jk}} = d_{imn} C_{mnljk} \quad (11)$$

in which P_i , ε_{jk} and σ_{jk} are polarization vector, strain and stress, respectively. The $e_{ijk}^{elc}/d_{ijk}^{elc}$ is clamped-ion piezoelectric coefficients (only electronic contributions). The $e_{ijk}^{ion}/d_{ijk}^{ion}$ is relax-ion piezoelectric coefficients as a realistic result (the sum of ionic and electronic contributions).

The Li-decorated monolayer FeX ($X=$ S, Se and Te) are centrosymmetric, which means that they have no

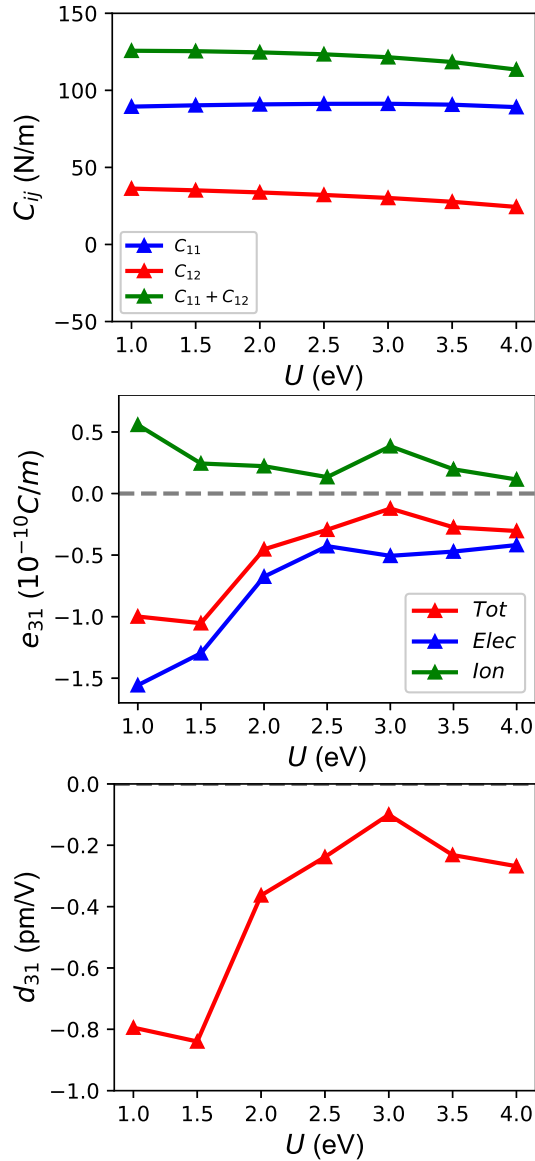


FIG. 12. (Color online) For Janus monolayer $\text{Li}_2\text{Fe}_2\text{SSe}$, the elastic constants C_{ij} , the piezoelectric stress coefficients (e_{31}) and the piezoelectric strain coefficients (d_{31}) as a function of U .

piezoelectricity. However, the monolayer $\text{Li}_2\text{Fe}_2\text{SSe}$ lacks glide mirror G_z symmetry, but has M_x and M_y mirrors symmetry, which gives only out-of-plane piezoelectricity, and the in-plane piezoelectricity will disappear. By using Voigt notation, the piezoelectric stress and strain tensors of monolayer $\text{Li}_2\text{Fe}_2\text{SSe}$ can be expressed as:

$$e = \begin{pmatrix} 0 & 0 & 0 \\ 0 & 0 & 0 \\ e_{31} & e_{31} & 0 \end{pmatrix} \quad (12)$$

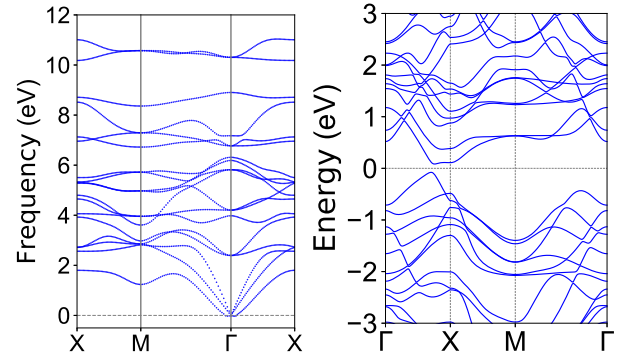


FIG. 13. (Color online) For Janus monolayer $\text{Li}_2\text{Fe}_2\text{SeTe}$, the phonon spectra (Left) and the energy band structure with GGA+SOC (Right).

$$d = \begin{pmatrix} 0 & 0 & 0 \\ 0 & 0 & 0 \\ d_{31} & d_{31} & 0 \end{pmatrix} \quad (13)$$

The e_{31} can be directly calculated by VASP code, and the d_{31} can be derived by Equation 11, Equation 12 and Equation 13.

$$d_{31} = \frac{e_{31}}{C_{11} + C_{12}} \quad (14)$$

Next, we use the primitive cell to calculate the e_{31} of Janus monolayer $\text{Li}_2\text{Fe}_2\text{SSe}$. Calculated results show that the e_{31} is -0.294×10^{-10} C/m with the ionic contribution 0.133×10^{-10} C/m and electronic one -0.427×10^{-10} C/m. It is found that the electronic and ionic parts have the opposite contributions, and the electronic contribution dominates the e_{31} . Based on Equation 14, the calculated d_{31} is -0.238 pm/V. The d_{31} of Janus monolayer $\text{Li}_2\text{Fe}_2\text{SSe}$ is higher than or comparable with ones of many 2D materials^{59–62}. The Coulomb interaction U effects on piezoelectric properties of monolayer $\text{Li}_2\text{Fe}_2\text{SSe}$ are also considered. The elastic constants C_{ij} , the piezoelectric stress coefficients (e_{31}) and the piezoelectric strain coefficients (d_{31}) as a function of U are plotted in Figure 12. A complex U dependence for e_{31} is observed, which leads to complicated U effects on d_{31} . It is found that the smallest d_{31} is -0.100 pm/V with $U=3$ eV.

IX. DISCUSSION AND CONCLUSION

In fact, Janus monolayer $\text{Li}_2\text{Fe}_2\text{SeTe}$ is also a QAH insulator. The energy difference between AFM and FM orders is 0.875 eV per unitcell, and the out-of-plane (001) direction is the easy one with MAE of $45 \mu\text{eV}/\text{Fe}$. The calculated C_{11} , C_{12} and C_{66} are 79.13 Nm^{-1} , 19.06 Nm^{-1} and 31.36 Nm^{-1} , which satisfy Born criteria of mechanical stability, indicating mechanical stability of monolayer $\text{Li}_2\text{Fe}_2\text{SeTe}$. The phonon spectra of $\text{Li}_2\text{Fe}_2\text{SeTe}$

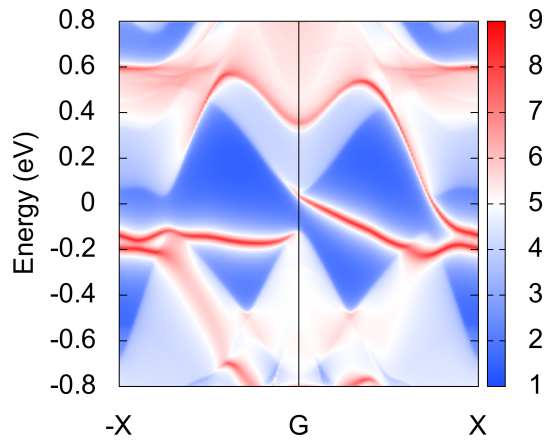


FIG. 14. (Color online) For Janus monolayer $\text{Li}_2\text{Fe}_2\text{SeTe}$, the topological edge states calculated along the (100) direction.

is plotted in Figure 13 with no imaginary frequency modes, confirming its dynamic stability. The AIMD simulations also confirm the thermal stability of monolayer LiFe_2SeTe at room temperature. The energy band structures and topological edge states of monolayer $\text{Li}_2\text{Fe}_2\text{SeTe}$ are shown in Figure 13 and Figure 14, respectively. The energy band gap is 161 meV, and the bulk states are connected by two chiral edge states, indicating Chern number $C=2$. The calculated d_{31} is 0.1 pm/V with e_{31} of 0.099×10^{-10} C/m.

In summary, using DFT+ U calculations, we have per-

formed a systematic investigation of the electronic, magnetic, topological and piezoelectric properties in Janus monolayer $\text{Li}_2\text{Fe}_2\text{SSe}$, which is predicted as an intriguing 2D PQAHI. It is proved that monolayer $\text{Li}_2\text{Fe}_2\text{SSe}$ is mechanically, dynamically and thermally stable. Also, the nontrivial properties are confirmed by a nonzero Chern number ($C=2$) and two gapless chiral edge states. Moreover, the monolayer $\text{Li}_2\text{Fe}_2\text{SSe}$ possesses out-of-plane magnetic anisotropy and very high Curie temperature (about 1000 K). The emergence of QAH effect in monolayer $\text{Li}_2\text{Fe}_2\text{SSe}$ is robust against strain and Hubbard U electronic correlation. The predicted d_{31} is comparable with ones of other 2D known materials. The predicted PQAHI in monolayer $\text{Li}_2\text{Fe}_2\text{SSe}$ is expected to work safely above room temperature, and provides a more promising platform for realizing low-dissipation topotronics devices, and provides possibility to use the piezotronic effect to control QAH effects.

ACKNOWLEDGMENTS

This work is supported by Natural Science Basis Research Plan in Shaanxi Province of China (2021JM-456). We are grateful to the Advanced Analysis and Computation Center of China University of Mining and Technology (CUMT) for the award of CPU hours and WIEN2k/VASP software to accomplish this work.

- ¹ K. V. Klitzing, G. Dorda and M. Pepper, Phys. Rev. Lett. **45**, 494 (1980).
- ² F. D. M. Haldane, Phys. Rev. Lett. **61**, 2015 (1988).
- ³ D. Q. Zhang, M. J. Shi, T. S. Zhu, D. Y. Xing, H. J. Zhang and J. Wang, Phys. Rev. Lett. **122**, 206401 (2019).
- ⁴ H. J. Zhang, Y. Xu, J. Wang and S. C. Zhang, Phys. Rev. Lett. **112**, 216803 (2014).
- ⁵ H. J. Zhang, J. Wang, G. Xu, Y. Xu and S. C. Zhang, Phys. Rev. Lett. **112**, 096804 (2014).
- ⁶ M. Z. Hasan and C. L. Kane, Rev. Mod. Phys. **82**, 3045 (2010).
- ⁷ X. L. Qi and S. C. Zhang, Rev. Mod. Phys. **83**, 1057 (2011).
- ⁸ R. Yu, W. Zhang, H. J. Zhang, S. C. Zhang, X. Dai and Z. Fang, Science **329**, 61 (2010).
- ⁹ C. Z. Chang, J. Zhang, X. Feng, J. Shen, Z. Zhang, M. Guo, K. Li, Y. Ou, P. Wei, L. L. Wang, Z. Q. Ji, Y. Feng, S. Ji, X. Chen, J. Jia, X. Dai, Z. Fang, S. C. Zhang, K. He, Y. Wang, L. Lu, X. C. Ma and Q. K. Xue, Science **340**, 167 (2013).
- ¹⁰ P. Lin, C. Pan and Z. L. Wang, Materials Today Nano **4**, 17 (2018).
- ¹¹ M. Dai, Z. Wang, F. Wang, Y. Qiu, J. Zhang, C. Y. Xu, T. Zhai, W. Cao, Y. Fu, D. Jia, Y. Zhou, and P. A. Hu, Nano Lett. **19**, 5416 (2019).
- ¹² W. Wu, L. Wang, Y. Li, F. Zhang, L. Lin, S. Niu, D. Chenet, X. Zhang, Y. Hao, T. F. Heinz, J. Hone and Z. L. Wang, Nature **514**, 470 (2014).
- ¹³ A. Y. Lu, H. Zhu, J. Xiao, C. P. Chuu, Y. Han, M. H. Chiu, C. C. Cheng, C. W. Yang, K. H. Wei, Y. Yang, Y. Wang, D. Sokaras, D. Nordlund, P. Yang, D. A. Muller, M. Y. Chou, X. Zhang and L. J. Li, Nat. Nanotechnol. **12**, 744 (2017).
- ¹⁴ H. Zhu, Y. Wang, J. Xiao, M. Liu, S. Xiong, Z. J. Wong, Z. Ye, Y. Ye, X. Yin and X. Zhang, Nat. Nanotechnol. **10**, 151 (2015).
- ¹⁵ L. Dong, J. Lou and V. B. Shenoy, ACS Nano, **11**, 8242 (2017).
- ¹⁶ R. X. Fei, W. B. Li, J. Li and L. Yang, Appl. Phys. Lett. **107**, 173104 (2015).
- ¹⁷ M. N. Blonsky, H. L. Zhuang, A. K. Singh and R. G. Hennig, ACS Nano, **9**, 9885 (2015).
- ¹⁸ S. D. Guo, Y. T. Zhu, W. Q. Mu and W. C. Ren, EPL **132**, 57002 (2020).
- ¹⁹ W. B. Li and J. Li, Nano Res. **8**, 3796 (2015).
- ²⁰ Dimple, N. Jena, A. Rawat, R. Ahammed, M. K. Mohanta and A. D. Sarkar, J. Mater. Chem. A **6**, 24885 (2018).
- ²¹ N. Jena, Dimple, S. D. Behere and A. D. Sarkar, J. Phys. Chem. C **121**, 9181 (2017).
- ²² M. T. Ong and E.J. Reed, ACS Nano **6**, 1387 (2012).
- ²³ A. A. M. Noor, H. J. Kim and Y. H. Shin, Phys. Chem. Chem. Phys. **16**, 6575 (2014).
- ²⁴ J. Tan, Y. H. Wang, Z. T. Wang, X. J. He, Y. L. Liu, B. Wang, M. I. Katsnelson and S. J. Yuan, Nano Energy **65**, 104058 (2019).

- ²⁵ J. H. Yang, A. P. Wang, S. Z. Zhang, J. Liu, Z. C. Zhong and L. Chen, *Phys. Chem. Chem. Phys.*, **21**, 132 (2019).
- ²⁶ S. D. Guo, W. Q. Mu, Y. T. Zhu and X. Q. Chen, *Phys. Chem. Chem. Phys.* **22**, 28359 (2020).
- ²⁷ S. D. Guo, X. S. Guo, X. X. Cai, W. Q. Mu and W. C. Ren, arXiv:2103.15141 (2021).
- ²⁸ G. Song, D. S. Li, H. F. Zhou et al., *Appl. Phys. Lett.* **118**, 123102 (2021).
- ²⁹ S. D. Guo, W. Q. Mu, Y. T. Zhu, S. Q. Wang and G. Z. Wang, *J. Mater. Chem. C* **9**, 5460 (2021).
- ³⁰ S. D. Guo, Y. T. Zhu, W. Q. Mu and X. Q. Chen, *J. Mater. Chem. C* DOI: 10.1039/D1TC01165K (2021)..
- ³¹ S. D. Guo, W. Q. Mu, X. B. Xiao and B. G. Liu, arXiv:2105.03004 (2021).
- ³² Q. L. Sun, Y. D. Ma and N. Kiuoussis, *Mater. Horiz.* **7**, 2071 (2020).
- ³³ Y. Li, J. H. Li, Y. Li, M. Ye, F. W. Zheng, Z. T. Zhang, J. H. Fu, W. H. Duan and Y. Xu, *Phys. Rev. Lett.* **125**, (2020).
- ³⁴ A. Y. Lu, H. Y. Zhu, J. Xiao et al., *Nature Nanotechnology* **12**, 744 (2017).
- ³⁵ Y. Deng, Y. Yu, Y. Song, J. Zhang, N. Z. Wang, Z. Sun, Y. Yi, Y. Z. Wu, S. Wu, J. Zhu, et al., *Nature* **563**, 94 (2018).
- ³⁶ L. Ma, B. Lei, N. Wang, K. Yang, D. Liu, F. Meng, C. Shang, Z. Sun, J. Cui, C. Zhu, et al., *Sci. Bull.* **64**, 653 (2019).
- ³⁷ B. Lei, L. Ma, N. Wang, C. Zhu, J. Cui, Z. Sun, D. Ma, H. Wang, M. Shi, J. Ying, et al., *Phys. Rev. B* **100**, 174519 (2019).
- ³⁸ E. Dagotto, *Rev. Mod. Phys.* **85**, 849 (2013).
- ³⁹ P. Hohenberg and W. Kohn, *Phys. Rev.* **136**, B864 (1964); W. Kohn and L. J. Sham, *Phys. Rev.* **140**, A1133 (1965).
- ⁴⁰ G. Kresse, *J. Non-Cryst. Solids* **193**, 222 (1995).
- ⁴¹ G. Kresse and J. Furthmüller, *Comput. Mater. Sci.* **6**, **15** (1996).
- ⁴² G. Kresse and D. Joubert, *Phys. Rev. B* **59**, 1758 (1999).
- ⁴³ J. P. Perdew, K. Burke and M. Ernzerhof, *Phys. Rev. Lett.* **77**, 3865 (1996).
- ⁴⁴ V. I. Anisimov, F. Aryasetiawan and A. I. Lichtenstein, *J. Phys. Condens. Mat.* **9**, 767 (1997).
- ⁴⁵ J. Heyd, G. E. Scuseria and M. Ernzerhof, *J. Chem. Phys.* **118**, 8207 (2003).
- ⁴⁶ A. Togo, F. Oba, and I. Tanaka, *Phys. Rev. B* **78**, 134106 (2008).
- ⁴⁷ Q. Wu, S. Zhang, H. F. Song, M. Troyer and A. A. Soluyanov, *Comput. Phys. Commun.* **224**, 405 (2018).
- ⁴⁸ A. A. Mostofia, J. R. Yatesb, G. Pizzif, Y.-S. Lee, I. Souza, D. Vanderbilt and N. Marzari, *Comput. Phys. Commun.* **185**, 2309 (2014).
- ⁴⁹ L. Liu, X. Ren, J. H. Xie, B. Cheng, W. K. Liu, T. Y. An, H. W. Qin and J. F. Hu, *Appl. Surf. Sci.* **480**, 300 (2019).
- ⁵⁰ X. Wu, D. Vanderbilt and D. R. Hamann, *Phys. Rev. B* **72**, 035105 (2005).
- ⁵¹ E. Mariani and F. V. Oppen, *Phys. Rev. Lett.* **100**, 076801 (2008).
- ⁵² J. Carrete, W. Li, L. Lindsay, D. A. Broido, L. J. Gallego and N. Mingo, *Mater. Res. Lett.* **4**, 204 (2016).
- ⁵³ E. Cadelano and L. Colombo, *Phys. Rev. B* **85**, 245434 (2012).
- ⁵⁴ E. Cadelano, P. L. Palla, S. Giordano, and L. Colombo, *Phys. Rev. B* **82**, 235414 (2010).
- ⁵⁵ C. Lee, X. Wei, J. W. Kysar, and J. Hone, *Science* **321**, 385 (2008).
- ⁵⁶ B. Huang, G. Clark, E. Navarro-Moratalla, D. R. Klein, R. Cheng, K. L. Seyler, D. Zhong, E. Schmidgall, M. A. McGuire, D. H. Cobden, W. Yao, D. Xiao, P. Jarillo-Herrero and X. Xu, *Nature* **546**, 270 (2017).
- ⁵⁷ N. Miao, B. Xu, L. Zhu, J. Zhou and Z. Sun, *J. Am. Chem. Soc.* **140**, 2417 (2018).
- ⁵⁸ C. Gong, L. Li, Z. Li, H. Ji, A. Stern, Y. Xia, T. Cao, W. Bao, C. Wang, Y. Wang, Z. Q. Qiu, R. J. Cava, S. G. Louie, J. Xia and X. Zhang, *Nature* **546**, 265 (2017).
- ⁵⁹ A. A. M. Noor, H. J. Kim and Y. H. Shin, *Phys. Chem. Chem. Phys.* **16**, 6575 (2014).
- ⁶⁰ M. T. Ong and E. J. Reed, *ACS Nano* **6**, 1387 (2012).
- ⁶¹ Y. Guo, S. Zhou, Y. Z. Bai, and J. J. Zhao, *Appl. Phys. Lett.* **110**, 163102 (2017).
- ⁶² L. Hu and X.R. Huang, *RSC Adv.* **7**, 55034 (2017).